

Article

Dynamic Effect of Input-Voltage Feedforward in Three-Phase Grid-Forming Inverters

Matias Berg *  and Tomi Roinila 

Electrical Engineering, Tampere University, 33720 Tampere, Finland; tomi.roinila@tuni.fi

* Correspondence: matias.berg@tuni.fi

Received: 30 April 2020; Accepted: 2 June 2020; Published: 7 June 2020



Abstract: Grid-connected and grid-forming inverters play essential roles in the utilization of renewable energy. One problem of such a converter system is the voltage deviations in the DC-link between the source and the inverter that can disrupt the inverter output voltage. A common method to prevent these voltage deviations is to apply an input-voltage feedforward control. However, the feedforward control has detrimental effects on the inverter dynamics. It is shown that the effect of the feedforward in the input-to-output dynamics is not ideal due to the delay in the digital control system. The delay affects the input-to-output dynamics at high frequencies, and only a minor improvement can be achieved by low-pass filtering the feedforward control signal. Furthermore, the feedforward control can remarkably affect the inverter input admittance, and therefore, impedance-based stability problems may arise at the DC interface. This paper proposes a method based on linearization and extra element theorem to model the effect of the feedforward control in the inverter dynamics. Experimental measurements are shown to demonstrate the effectiveness of the proposed model.

Keywords: VSI; DC dynamics; input-to-output dynamics; input admittance; feedforward; grid forming; extra element theorem

1. Introduction

Grid-connected and grid-forming inverters play essential roles in the utilization of renewable energy. Photovoltaic panels, fuel cells, and battery energy storage systems produce direct current. In order to distribute the energy from such sources through a utility grid, a grid-connected inverter is required. Grid-forming inverters, on the other hand, are required for utilizing the energy in inverter-based microgrids. In all these systems, the operation of the inverters is strongly dependent on the applied DC source. The source and its dynamics may greatly vary thus affecting the inverter input dynamics, and consequently, the produced power quality in the AC side.

Recent studies have presented several methods to analyze the stability of grid-connected power-electronics systems. In [1], a grid-connected converter is modeled by a modular state-space model, and a transformation matrix from the synchronous reference frame to the stationary reference frame is presented. Many studies have applied impedance-based stability criterion; the converter output impedance is measured or modeled and then compared to the grid impedance at the point of common coupling. In [2], the stability of an output-voltage-controlled inverter and an active rectifier is addressed by applying the generalized Nyquist stability criterion (GNC) on the return-ratio matrix of the impedances. The GNC has been used on stability analysis of grid-connected inverters and the focus has been on different topics, such as effect of the DC-link control dynamics [3], the active damping [4], and a virtual synchronous machine implementation in the converter control system [5].

Recently, more attention has been paid to analyzing the dynamics at the DC-interface. In [6], the input impedance of a three-phase VSI was studied in different control modes, such as droop control and DC voltage control. The effect of the DC link and front-end converter on the dynamic

modes of grid-connected PV energy system was modeled in [7]. The stability of the interconnected three-phase-balanced-voltage PWM rectifier and LLC resonant converter was investigated in [8] by modeling the converter terminal DC impedances at the point of common coupling. In [9], the interactions between a boost converter and a VSI in grid-connected and islanded mode was studied, and it was found out that a good damping is achieved on the DC side when the DC voltage is controlled by the VSI. Past studies have also presented DC-impedance models of dq-domain-controlled three-phase grid-feeding PV inverters [4] and grid-forming inverters [10]. However, there are still many issues to be addressed regarding the DC dynamics of three-phase microgrid inverters, such as the harmonic spectrum filtration for current-sensor measurements [11]. One of the issues is related to the inverter input-voltage feedforward.

In the input-voltage feedforward, the measured and normalized input voltage divides the converter duty ratio in order to prevent disturbances from the input voltage affecting the output. However, at the same time, the DC input admittance of the inverter is affected. Due to the changes in the converter dynamics, modeling of the feedforward is essential.

In the case of DC-DC converters, the topic has been addressed thoroughly. In [12,13], the input-voltage-feedforward-controlled buck converter was compared systemically with the voltage-mode control and the peak-current-mode control. The feedforward was shown to significantly reduce the input-to-output dynamics gain compared to the voltage-mode-control. It was shown that with the feedforward control the input admittance corresponds to the ideal input admittance that is, in the case of a buck converter, close to the negative ratio of the steady state input current and input voltage. In [14], a dynamic ramp was used to implement the input-voltage feedforward control. However, the analyzed DC-DC converters [12–14] were controlled with analog electronics. Therefore, the delay that is in digital control systems was not considered.

The utilization of input-voltage feedforward with three-phase converters has been presented in some papers. In [15,16], the input-voltage feedforward was drawn in the control diagram; however, it was not further analyzed. It was stated in [17–19] that the input-voltage feedforward decouples the AC dynamics from the DC dynamics, and therefore, the DC dynamics were not included in the modeling. In [20], the division by the input voltage was included in a state space model. However, the delay associated with the control system was not discussed.

This paper presents a dynamic analysis of the input-voltage feedforward in grid-forming inverters. In the analysis, the feedforward is linearized to a fixed operating point. The input admittance is modeled by the ideal input admittance model that is a special parameter known from the analysis of DC/DC converters. Applying the analysis, the effect of the feedforward can be included in the transfer matrices, thus making it possible to predict the impedance-based stability more accurately and to model the effect of the DC voltage deviations on the AC side. Furthermore, low-pass filtering the feedforward signal control is investigated to examine if there is a simple way to improve the input-to-output dynamics.

The remainder of this paper is structured as follows. Section 2 examines the dynamic model of the grid-forming inverter with the traditional current and voltage feedbacks. Section 3 derives the model of the feedforward and analyses the input-to-output dynamics. The input-voltage-feedforward-affected input admittance is introduced in Section 4. Section 5 examines a low-pass filter implementation in the feedforward. In Section 6, experimental measurements are used to verify the proposed models. Section 7 shows how the proposed ideal-input-admittance model can be linked to existing models. Conclusions are drawn in Section 8.

2. System Dynamic Model

In this section, the dynamic model for the grid-forming inverter is investigated. The open-loop model and the traditional cascaded current and voltage control loops are considered.

Figure 1 shows a simplified block diagram of a grid-forming inverter. The traditional cascaded inductor current and output voltage feedback are implemented on the AC side. In the unterminated

model, the load is an ideal current sink and the power is fed from a DC voltage source. The deviations in the DC voltage are compensated by dividing the inverter control signal with the normalized DC voltage. The DC voltage is normalized because in the nominal condition without the feedforward the current controllers output, c , equals the duty ratio d . Bold notation denotes a vector that consists of direct and quadrature components. If the vector notation is not used, subscripts “d” and “q” are used to denote the direct and quadrature components, respectively. This normalization would not be required if the dynamics were modeled with a PWM reference voltage instead of the duty ratio.

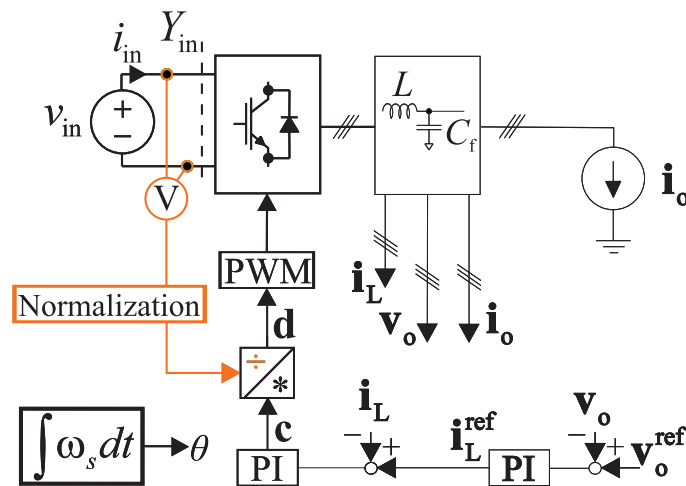


Figure 1. Simplified block diagram of the analyzed converter.

The open-loop transfer-function presentation from the system inputs to the system outputs can be given as [10]:

$$\begin{bmatrix} \hat{i}_{in} \\ \hat{i}_L \\ \hat{v}_o \end{bmatrix} = \begin{bmatrix} Y_{in} & T_{oi} & G_{ci} \\ G_{iL} & G_{oL} & G_{cL} \\ G_{io} & -Z_o & G_{co} \end{bmatrix} \begin{bmatrix} \hat{v}_{in} \\ \hat{i}_o \\ \hat{d} \end{bmatrix} \quad (1)$$

where Y_{in} , G_{iL} , and G_{io} denote the input admittance, the input-to-inductor current transfer matrix, and the input-to-output transfer matrix, respectively. T_{oi} , G_{oL} , and Z_o stand for the output-to-input transfer matrix, the output-to-inductor current transfer matrix, and the output impedance matrix, respectively. The control-related transfer matrices G_{ci} , G_{cL} and G_{co} denote the control-to-input current, the control-to-inductor current, and the control-to-output voltage transfer matrices, respectively. The open-loop transfer-function matrices are used in Figure 2a with the addition of the current controller G_{cc} and the voltage controller G_{vc} transfer matrices to form the closed-loop system. The system parameters and operating point values are given in Table 1 where the synchronous-reference-frame-steady-state values are defined as peak values. The abbreviation ESR stands for the equivalent series resistance. The input-voltage feedforward is modeled by G_{vin}^{FF} .

The division by the input-voltage feedforward is highlighted in orange in Figure 2a. Figure 2b shows the input and the output dynamics of the system with additional elements R and Z_E that will be used to analyze the effect of a low-pass filter in Section 5. In Sections 2 and 3, Z_E is made open, and therefore, \hat{v}_{in}^* equals \hat{v}_{in} . The dynamic presentation for the input-voltage feedforward is derived by two methods in the next section.

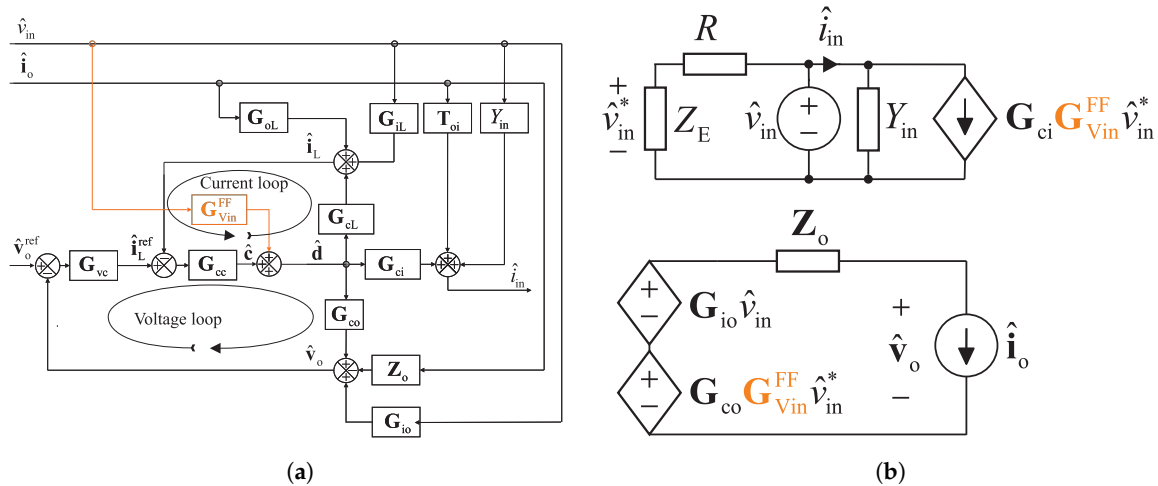


Figure 2. (a) Control block diagram of the inverter system. (b) Circuit diagram of the input and the output dynamics with the feedforward.

Table 1. Parameters and operating point values.

Parameter	Symbol	Value	Parameter	Symbol	Value
Input voltage	V_{in}	416 V	Input current	I_{in}	12.1 A
Output voltage d component	V_{od}	169.7 V	Output voltage q component	V_{oq}	0 V
Output current d component	I_{od}	19.64 A	Output current q component	I_{oq}	0 A
Inductor current d component	I_{Ld}	19.65 A	Inductor current q component	I_{Lq}	2.24 A
Duty ratio d component	D_d	0.4045 A	Duty ratio q component	D_q	0.05 A
Switching frequency	f_s	10 kHz	Synchronous frequency	ω_s	$2\pi 60$ rad/s
Filter capacitor capacitance	C_f	35 μ F	Filter inductance	L	2.5 mH
Filter capacitor ESR	r_{Cf}	0.1 Ω	L ESR	r_L	0.025 Ω
Current controller P gain	K_{p-c}	0.028 Ω	Current controller I gain	K_{i-c}	17.8 VA ⁻¹ s ⁻¹
Voltage controller P gain	K_{p-v}	0.040 Ω^{-1}	Voltage controller I gain	K_{i-v}	10.0 AV ⁻¹ s ⁻¹

3. Input-Voltage Feedforward and Input-to-Output Dynamics

This section considers the inverter input-to-output dynamics with the feedforward. First, a transfer matrix from the input voltage to the duty ratios is derived. Then, the detrimental effect of the delay with the input-voltage feedforward is examined.

3.1. Linearization Approach

The dynamics of the input-voltage feedforward can be solved by linearizing the division of the current controller output d and q components, c_d and c_q , by the input voltage with respect to the input voltage v_{in} :

$$\frac{\delta}{\delta v_{in}} V_{in} \frac{c_d}{v_{in}} \hat{v}_{in} = V_{in} \frac{-D_d}{V_{in}^2} \hat{v}_{in} = \frac{-D_d}{V_{in}} \hat{v}_{in} \tag{2}$$

$$\frac{\delta}{\delta v_{in}} V_{in} \frac{c_q}{v_{in}} \hat{v}_{in} = V_{in} \frac{-D_q}{V_{in}^2} \hat{v}_{in} = \frac{-D_q}{V_{in}} \hat{v}_{in} \tag{3}$$

where V_{in} , D_d , and D_q are the steady-state values of the input voltage and duty-ratio d and q components, respectively. The hat is used to denote small-signal values. The results can be collected to a transfer matrix

$$\mathbf{G}_{V_{in}}^{FF} = \begin{bmatrix} \frac{-D_d}{V_{in}} \\ \frac{-D_q}{V_{in}} \end{bmatrix} \tag{4}$$

which presents how \hat{v}_{in} affects \hat{d}_d and \hat{d}_q . The input-voltage-feed-forward-affected input-to-output dynamics are calculated according to Figure 2b:

$$\mathbf{G}_{io}^{Vin-FF} = \mathbf{G}_{io} + \mathbf{G}_{co} \mathbf{G}_{Vin}^{FF} \quad (5)$$

3.2. Mitigating the Effect of Input-Voltage Deviations

In the ideal case, the feedforward would reduce the gain of the input-voltage-to-output voltage dynamics \mathbf{G}_{io} to zero. Therefore, the gain of the feed-forward-affected input-to-output dynamics \mathbf{G}_{io}^{Vin-FF} should be zero:

$$\mathbf{G}_{io}^{Vin-FF} = \mathbf{G}_{io} + \mathbf{G}_{co} \mathbf{G}_{Vin}^{FF} = 0 \quad (6)$$

The ideal feedforward gain can be given as follows

$$\mathbf{G}_{Vin}^{FF} = -\mathbf{G}_{co}^{-1} \mathbf{G}_{io} \quad (7)$$

In a synchronous-switching buck-type converter, the transfer functions from the input voltage and the duty-ratio to the output have the dynamics of the filter, and the dynamics differ only at the DC gain ($s = 0$) if the voltage drop over the components is assumed small. Therefore, the following analysis can be done by using the DC gains. The cross-coupling gains of the control-to-output transfer function are approximated to be very small:

$$\mathbf{G}_{co}(0) = \begin{bmatrix} G_{co-d}(0) & G_{co-qd}(0) \\ G_{co-dq}(0) & G_{co-q}(0) \end{bmatrix} \approx \begin{bmatrix} V_{in} & 0 \\ 0 & V_{in} \end{bmatrix} \quad (8)$$

$$\mathbf{G}_{io}(0) = \begin{bmatrix} G_{io-d}(0) \\ G_{io-q}(0) \end{bmatrix} \approx \begin{bmatrix} D_d \\ D_q \end{bmatrix} \quad (9)$$

The resulting ideal input-voltage feed-forward transfer function is the same as the previous linearization (4) result of the input voltage division:

$$\mathbf{G}_{Vin}^{FF}(0) = -\mathbf{G}_{co}^{-1}(0) \mathbf{G}_{io}(0) = \begin{bmatrix} \frac{-D_d}{V_{in}} \\ \frac{-D_q}{V_{in}} \end{bmatrix} \quad (10)$$

3.3. Effect of the Delay

In the previous analysis, the delay from the digital control system was neglected. Now the delay is modeled by a third-order Padé approximation [4]:

$$G_{del} = \frac{1 - s \frac{T_d}{2} + s^2 \frac{T_d^2}{12} - s^3 \frac{T_d^3}{120}}{1 + s \frac{T_d}{2} + s^2 \frac{T_d^2}{12} + s^3 \frac{T_d^3}{120}} \quad (11)$$

where $T_d = 1.5T_s$ is the delay length in seconds, and T_s is the switching cycle, $1/f_s$. The delay matrix that is used with the multivariable control-related transfer matrices is defined as follows

$$\mathbf{G}_{del} = \begin{bmatrix} G_{del} & 0 \\ 0 & G_{del} \end{bmatrix} \quad (12)$$

The input-feedforward affected input-to-output dynamics with the delay is given by

$$\mathbf{G}_{io}^{Vin-FF} = \mathbf{G}_{io} + \mathbf{G}_{co} \mathbf{G}_{Vin}^{FF} \mathbf{G}_{del} \quad (13)$$

Figure 3a,b show the frequency responses of the input-to-output dynamics without the feedforward and with the feedforward using the model in (13). The input-voltage feedforward clearly reduces the gain of the input-to-output dynamics both in the d and q components at low frequencies. However, due to the phase shift caused by the delay, the effect of the feedforward becomes detrimental at 1111 Hz because the magnitude is higher with the feedforward than without it. In addition to the modeled frequency responses, Figure 3 shows a verification from a real-time hardware-in-the-loop (HIL) simulation that was performed on Typhoon HIL model 402.

The frequency where the feedforward becomes detrimental can be solved by finding the phase shift θ in the feedforward signal that causes the absolute values of the input-to-output dynamics with and without the feedforward to equal:

$$|G_{io-d}| = \left| G_{io-d} + G_{co-d} G_{V_{in-d}}^{FF} (\cos(\theta) + j \sin(\theta)) \right| \quad (14)$$

where, $\cos(\theta) + j \sin(\theta)$ is used to model the phase shift at the angle θ by its real and imaginary parts according to the Euler's formula. The aforementioned similarity in the input-to-output dynamics and the control-to-output dynamics is used to simplify the analysis. The transfer functions are approximated by their DC gains:

$$|D_d| = \left| D_d + V_{in} \frac{-D_d}{V_{in}} (\cos(\theta) + j \sin(\theta)) \right| \quad (15)$$

$$D_d^2 = D_d^2 - 2D_d^2 \cos(\theta) + D_d^2 \cos^2(\theta) + D_d^2 \sin^2(\theta) \quad (16)$$

where θ can be solved as:

$$\theta = \pm n60^\circ, \quad n \in \mathbb{N} \quad (17)$$

The delay causes a negative phase shift, and the smallest negative phase shift required is -60° . The frequency f_{-60° where the phase shift takes place is

$$f_{-60^\circ} = \frac{60^\circ}{kT_s 360^\circ} = \frac{f_s}{6k} = \frac{f_s}{9}, \quad |k = 1.5 \quad (18)$$

where k denotes the ratio between the delay T_d and the switching cycle T_s . If T_d equals $1.5 T_s$, the frequency f_{-60° is 1111 Hz. Figure 4 shows the ratio of $G_{io-d}^{V_{in-FF}}$ and G_{io-d} with the delays of $1.5T_s$ and $3T_s$ and the analytically solved frequencies for the corresponding delay lengths. As the figure shows, (18) gives correctly the frequency where the input-to-output transfer function has a equal magnitude with the feedforward and without it and the the delay phase shift is -60° . These findings highlight the fact that, due to the delay, the feedforward provides no perfect decoupling from the input-voltage deviations, and the delay must be modeled. In Section 5, a first-order low-pass filter is used to mitigate the delay effect.

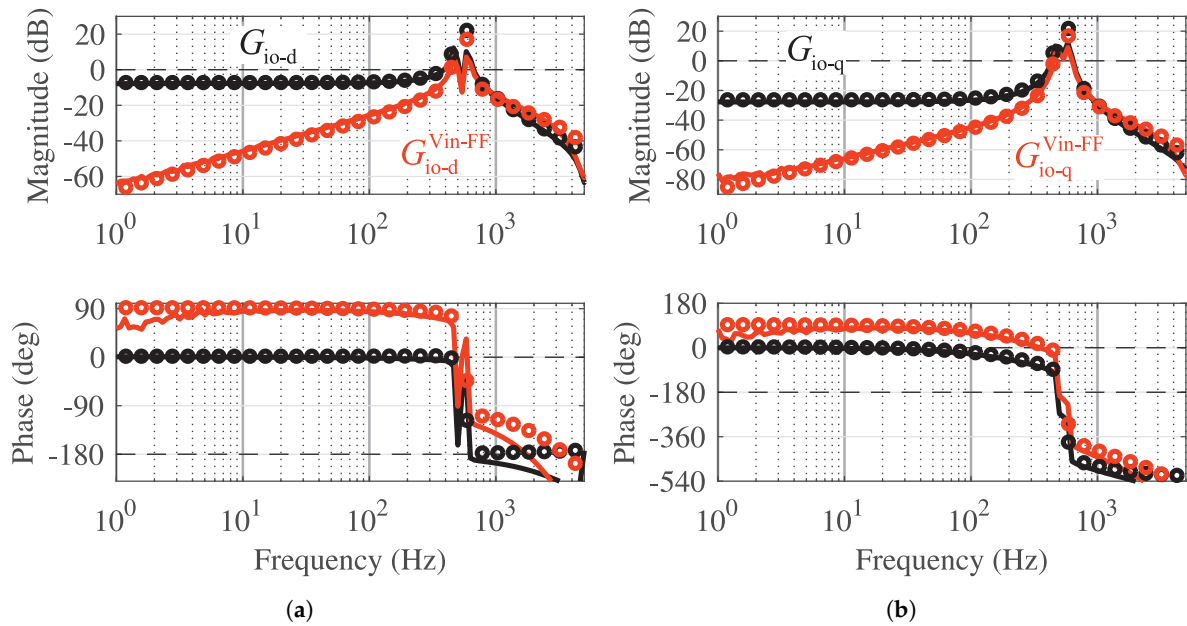


Figure 3. Modeled (dots) and HIL simulation (line) open-loop input-to-output dynamics (a) d component and (b) q component.

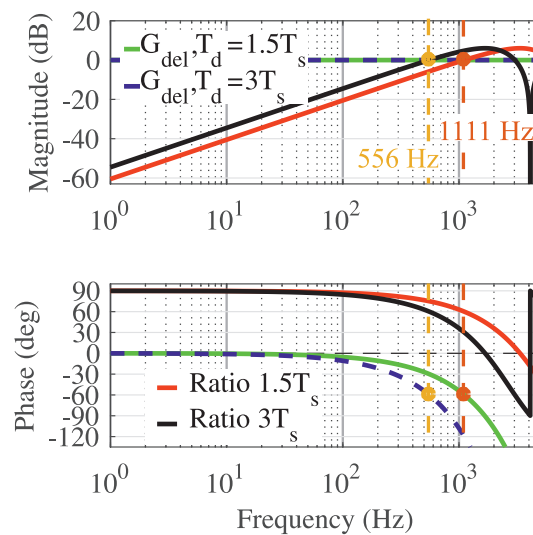


Figure 4. The ratios of $G_{io-d}^{Vin-FF} / G_{io-d}$ and the Padé approximations of the delay with the delay length of $1.5T_s$ and $3T_s$.

4. Input Admittance

This section examines the input admittance with the feedforward. First, the ideal input admittance that is a special parameter known from the modeling of DC-DC converters is derived. Then, the input admittance is analyzed with the inductor-current feedback and the output-voltage feedback.

4.1. Ideal Input Admittance

The ideal input admittance has been applied in modeling the source effect on the control-to-output dynamics in DC-DC converters [13,21–23] and the ideal-input-admittance components in three-phase inverters [24]. From the modeling of DC-DC converters [13], it is known that with the input-voltage feedforward the input admittance corresponds to the ideal input admittance. The ideal input admittance is a special parameter that corresponds to a formulation (null-double-injection admittance) [22] from the extra element theorem [25]. Next, the ideal input admittance is derived similarly for the three-phase

voltage-source inverter (VSI) as for DC-DC converters [13,23]. The ideal input admittance for the three-phase VSI can be given as

$$Y_{in-\infty} = Y_{in} - \mathbf{G}_{ci} \mathbf{G}_{co}^{-1} \mathbf{G}_{io} \quad (19)$$

where the inverse of \mathbf{G}_{co} implies that the ideal input admittance corresponds to a case where the output-voltage controller is infinitely fast. In order to simplify the analysis, the resistive losses and the cross coupling between the d and q channels are neglected. The transfer functions of (19) can be approximated as follows

$$Y_{in} \approx \frac{(3C_f V_{od}^2 + 3C_f V_{oq}^2) s}{2C_f L V_{in}^2 s^2 + 2V_{in}^2} \quad (20)$$

$$\mathbf{G}_{ci} \approx \begin{bmatrix} G_{ci-d} & G_{ci-q} \end{bmatrix} \approx \begin{bmatrix} \frac{3C_f L I_{od} s^2 + 3C_f V_{od} s + 3I_{od}}{2C_f L s^2 + 2} & \frac{3C_f L I_{oq} s^2 + 3C_f V_{oq} s + 3I_{oq}}{2C_f L s^2 + 2} \end{bmatrix} \quad (21)$$

$$\mathbf{G}_{co} \approx \begin{bmatrix} \frac{V_{oq}}{C_f L V_{in} s^2 + V_{in}} & 0 \\ 0 & \frac{V_{od}}{C_f L V_{in} s^2 + V_{in}} \end{bmatrix} \quad (22)$$

$$\mathbf{G}_{io} \approx \begin{bmatrix} \frac{V_{in}}{C_f L s^2 + 1} \\ \frac{V_{in}}{C_f L s^2 + 1} \end{bmatrix} \quad (23)$$

The ideal input admittance (19) can be shown to be:

$$Y_{in-\infty} \approx -\frac{3 I_{od} V_{od}}{2 V_{in}^2} - \frac{3 I_{oq} V_{oq}}{2 V_{in}^2} \approx \frac{3 I_{od} D_d}{2 V_{in}} - \frac{3 I_{oq} D_q}{2 V_{in}} \quad (24)$$

The result is in line with the ideal input admittance of DC-DC converters [13,23]. Despite the approximations, the model is adequate as it will be shown in Section 4.2.

4.2. Closed-Loop Input Admittance with the Input-Voltage Feedforward

The inductor-current feedback and the output-voltage feedback are formed according to Figure 2a. The delay is neglected in the following approximation. However, when the approximation is not used and the delay is modeled, each of the control-related transfer matrices \mathbf{G}_{ci} , \mathbf{G}_{cL} and \mathbf{G}_{co} are multiplied from right by \mathbf{G}_{del} given in (12). The multi-variable inductor-current control-loop gain is given by

$$\mathbf{L}_{outC} = \mathbf{G}_{cc} \mathbf{G}_{cL} \quad (25)$$

For simplicity, only the closed-loop input admittance is studied among the transfer functions. At first, the inductor-current control loop is closed

$$Y_{in}^{sec} = Y_{in} + \mathbf{G}_{ci} \left(-\mathbf{G}_{cc} (\mathbf{I} + \mathbf{L}_{outC})^{-1} \mathbf{G}_{iL} - \overbrace{\mathbf{G}_{co}^{-1} \mathbf{G}_{io}}^{\mathbf{G}_{Vin}^{FF}} \right) \quad (26)$$

where the superscript *sec* denotes that the secondary feedback loop is closed. The equation can be manipulated to a form that resembles the asymptotic-gain model. First, (26) is multiplied on the both sides from left by $(\mathbf{I} + \mathbf{L}_{outC})$

$$\begin{aligned}
 (\mathbf{I} + \mathbf{L}_{\text{outC}}) Y_{\text{in}}^{\text{sec}} &= \mathbf{I} Y_{\text{in}} + \mathbf{I} \mathbf{G}_{\text{ci}} \mathbf{G}_{\text{Vin}}^{\text{FF}} + \mathbf{L}_{\text{outC}} \overbrace{(\mathbf{Y}_{\text{in}} + \mathbf{G}_{\text{ci}} \mathbf{G}_{\text{Vin}}^{\text{FF}})}^{Y_{\text{in}-\infty}} \\
 &\quad - \mathbf{I} \mathbf{G}_{\text{ci}} \mathbf{G}_{\text{cc}} (\mathbf{I} + \mathbf{L}_{\text{outC}})^{-1} \mathbf{G}_{\text{iL}} - \mathbf{L}_{\text{outC}} \mathbf{G}_{\text{ci}} \mathbf{G}_{\text{cc}} (\mathbf{I} + \mathbf{L}_{\text{outC}})^{-1} \mathbf{G}_{\text{iL}}
 \end{aligned}
 \tag{27}$$

Rearranging the terms, the expression for $Y_{\text{in}-\infty}$ can be found. Then both sides are multiplied from left by $(\mathbf{I} + \mathbf{L}_{\text{outC}})^{-1}$ resulting:

$$\begin{aligned}
 \overbrace{(\mathbf{I} + \mathbf{L}_{\text{outC}})^{-1} (\mathbf{I} + \mathbf{L}_{\text{outC}})}^{=\mathbf{I}} Y_{\text{in}}^{\text{sec}} &= \overbrace{(\mathbf{I} + \mathbf{L}_{\text{outC}})^{-1} \mathbf{I} Y_{\text{in}}}^{\approx 0} + \overbrace{(\mathbf{I} + \mathbf{L}_{\text{outC}})^{-1} \mathbf{I} \mathbf{G}_{\text{ci}} \mathbf{G}_{\text{Vin}}^{\text{FF}}}^{\approx 0} \\
 &\quad + \overbrace{(\mathbf{I} + \mathbf{L}_{\text{outC}})^{-1} \mathbf{L}_{\text{outC}} Y_{\text{in}-\infty}}^{\approx \mathbf{I}} \\
 &\quad - \overbrace{(\mathbf{I} + \mathbf{L}_{\text{outC}})^{-1} (\mathbf{I} + \mathbf{L}_{\text{outC}}) \mathbf{G}_{\text{ci}} \mathbf{G}_{\text{cc}} (\mathbf{I} + \mathbf{L}_{\text{outC}})^{-1} \mathbf{G}_{\text{iL}}}^{\approx 0}
 \end{aligned}
 \tag{28}$$

where it is assumed that the magnitude of the multivariate loop-gain (25) is very high. Equation (28) shows that $Y_{\text{in}}^{\text{sec}} \approx Y_{\text{in}-\infty}$. The same analysis can be done for the output-voltage feedback

$$Y_{\text{in}}^{\text{tot}} = Y_{\text{in}}^{\text{sec}} - \mathbf{G}_{\text{ci}}^{\text{sec}} \overbrace{(\mathbf{I} + \mathbf{G}_{\text{co}}^{\text{sec}} \mathbf{G}_{\text{vc}})^{-1} \mathbf{G}_{\text{io}}^{\text{sec}}}^{\approx 0} \approx Y_{\text{in}-\infty}
 \tag{29}$$

With the input-voltage feedforward, the input admittance remains unchanged although the inductor current and output voltage feedback loops are closed, and it corresponds to the ideal input admittance defined in (24).

Figure 5a shows the open-loop input admittance with and without the feedforward. The feedforward clearly increases the input admittance to $Y_{\text{in}-\infty}$. However, due to the delay in the sampling and digital control, the phase drops and the gain changes at high frequencies. When the current and the output-voltage control loops are closed, the input impedance appears as a constant power load within the control bandwidth as Figure 5b shows. Nevertheless, the input-voltage feedforward keeps the admittance in $Y_{\text{in}-\infty}$ even outside the voltage controller-bandwidth. With the feedforward, the region where the phase is -180° is wider than without the feedforward. The phase above -90° can cause impedance-based stability issues at the DC interface of the converter.

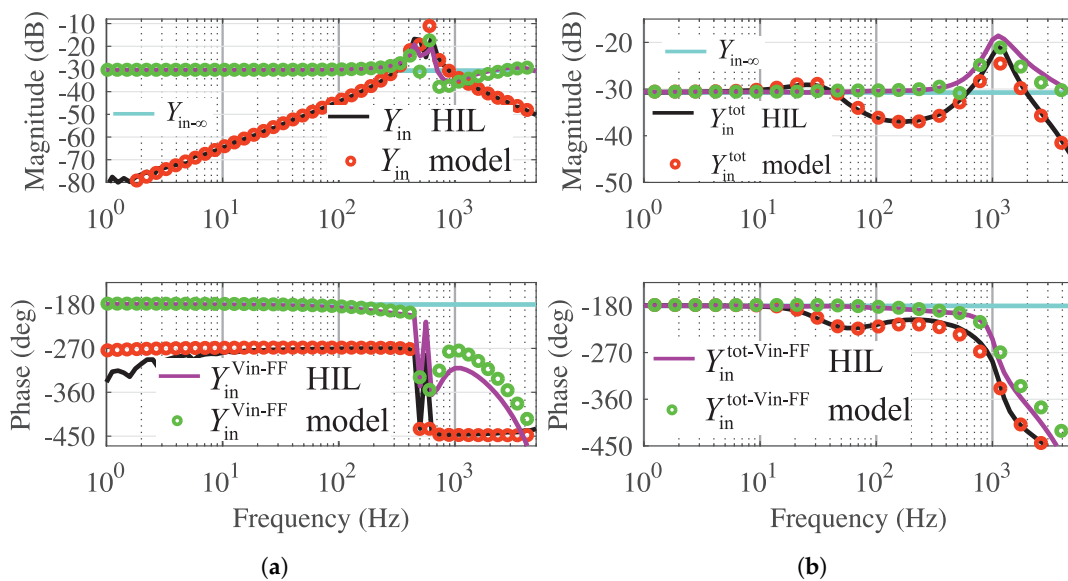


Figure 5. (a) Open-loop input admittance with and without the input voltage feedforward. (b) Closed-loop input admittance with and without the input voltage feedforward.

5. Bandwidth Considerations

As it can be seen from the frequency responses in Figures 3a,b, and 4, the feedforward does not minimize the gain of the input-to-output dynamics at all frequencies due to the delay. Instead, the gain is increased at frequencies higher than $f_s/9$.

A high frequency stability problem between a HVDC Converter and AC grid due to the AC output-voltage feedforward was reported in [26]. The problem was solved by implementing a low-pass filter in the feedforward. Consequently, implementing a low-pass filter in the input-voltage feedforward to reduce the high frequency gain is analyzed. The negative effect of the feedback is studied by inspecting the ratio of the input-to-output dynamics with and without the feedforward.

The extra-element method given in [25,27] is a technique to facilitate modeling of systems consisting of linear transfer functions, and the theorem has been used, for example, in tuning an active filter in a wind-power-plant system [28]. In the present paper, the extra element theorem can be used to give a formulation for the system in Figure 2b where adding the extra element Z_E implements a low-pass-filtered input-voltage feedforward:

$$G_d = G_{sc-d} \frac{1 + \frac{Z_E}{Z_{E-n}}}{1 + \frac{Z_E}{Z_{E-d}}}, \quad G_d \Big|_{Z_E \rightarrow 0} = G_{io-d} \quad (30)$$

$$G_{sc-d} = G_{io-d} \quad (31)$$

$$Z_{E-d} = R = 1\Omega \quad (32)$$

$$Z_{E-n} = \frac{R}{1 + \frac{1}{G_{io-d}} G_{co-d} G_{Vin-d}^{FF} G_{del} + \frac{1}{G_{io-d}} G_{co-qd} G_{Vin-q}^{FF} G_{del}} \quad (33)$$

where G_{sc-d} is the transfer function from the input voltage to the output voltage when the extra element, Z_E , is made a short. G_d is the analyzed transfer function with the influence of Z_E . The single-injection driving point impedance, Z_{E-d} , is the impedance seen from the extra element when the input voltage is replaced by a short. The null-double injection impedance, Z_{E-n} , is the impedance seen from the extra element when the input voltage nulls the effect of the measurement from the extra element on the output voltage.

The low-pass filter is modeled by impedances R and Z_E . R is a resistor. Z_E is the reactance of a capacitor

$$Z_E = -jX_C = -j\frac{1}{\omega C} \quad (34)$$

where ω is the angular frequency and C the extra-element capacitor capacitance. When Z_E is short-circuited, v_{in}^* equals v_{in} and there is no low-pass filter as Figure 2b shows. By changing the capacitor values, the cut-off frequency of the RC-low-pass filter can be changed. The impedances are only used as a tool to model the cut-off frequency of a digital low-pass filter, and therefore, R is set to 1Ω .

The ratio describing how the extra element affects the system dynamics can be given as follows:

$$K = \left| \frac{1 + \frac{Z_E}{Z_{E-n}}}{1 + \frac{Z_E}{Z_{E-d}}} \right| = \left| \frac{1 + \frac{-jX_C}{\Re(Z_{E-n}) + j\Im(Z_{E-n})}}{1 + \frac{-jX_C}{1}} \right|, \quad K \in \mathbb{R}_{>0} \quad (35)$$

X_C can be solved as a function of desired K by manipulating (35) to the second-order equation form that is easy to solve:

$$X_C^2 \left[1 - K^2 \Re \{Z_{E-n}\}^2 - K^2 \Im \{Z_{E-n}\}^2 \right] + X_C [-2\Im \{Z_{E-n}\}] + (1 - K^2) \left[\Re \{Z_{E-n}\}^2 + \Im \{Z_{E-n}\}^2 \right] = 0 \quad (36)$$

The equation has two solutions, X_{C-1} and X_{C-2} . The required cut-off frequency, f_{cut} , for the low-pass filter is given by

$$f_{cut} = \frac{\omega}{2\pi} X_C(\omega) \quad (37)$$

Figure 6a shows the solutions to (36) as bode plots. Only real-solutions, where the phase is 0° , can be implemented. In Figure 6a, X_{C-1} is zero below 3360 Hz which implies that design criterion is met only when the feedforward is not used. Between 1111 Hz and 3360 Hz, the phase of solution X_{C-2} is -180° which means that the low-pass filter should have a right-half-plane pole that obviously cannot be implemented. This result implies that a first-order low-pass filter cannot be used to mitigate the detrimental effect from the delay in the frequency range between 1111 Hz and 3360 Hz. However, solution X_{C-2} can be implemented on frequencies below 1111 Hz.

A low-pass filter is implemented so that the magnitude with and without the feedforward is the same at 250 Hz. The required cut-off frequency is calculated at 250 Hz from X_{C-2} shown in Figure 6a. The required cut-off frequency is 123.5 Hz. Figure 6b shows G_{io-d} and the low-pass-filtered input-voltage-feedforward affected input-to-output dynamics d component, $G_{io-d}^{VinFF-LP}$. As it can be seen, the transfer functions have the same gain at 250 Hz. However, this may not be advantageous because the effect of the feedforward is highly reduced at the low frequencies.

More benefits could be achieved from the input admittance point of view. In order to analyze the effect of the low-pass filter on the input admittance, the elements G_{sc} and Z_{E-n} are redefined :

$$G_{sc} = Y_{in} \quad (38)$$

$$Z_{E-n} = \frac{R}{1 + \frac{1}{Y_{in}} G_{ci-d} G_{Vin-d}^{FF} G_{del} + \frac{1}{Y_{in}} G_{ci-q} G_{Vin-q}^{FF} G_{del}} \quad (39)$$

As an example we can assume that the input admittance should be only 3 dB higher with the feedforward than without the feedforward at 200 Hz. The solution can be seen in Figure 7a, which shows that X_{C-2} is realizable at 200 Hz and it corresponds to a low-pass filter with a cut-off frequency of 37.4 Hz. The upper gain figure in Figure 7b shows the comparison of the models of the input admittance Y_{in} , the input admittance with the feedforward Y_{in}^{VinFF} , and the input admittance with the low-pass-filtered feedforward $Y_{in}^{VinFF-LP}$ in the open loop. The gain difference at 200 Hz is exactly 3 dB. However, the lower figure in Figure 7b shows that the difference is 2 dB, which is due to the current and the voltage controllers.

The benefit from the low-pass filter in the closed-loop input admittance is clearly visible. However, as it is shown in Figure 6b, the feedforward effect on the input-to-output dynamics is highly reduced by a low-pass filter. In the next section, it will be shown that the DC link capacitor can increase the input admittance significantly, and the feedforward effect on the input admittance could become negligible.

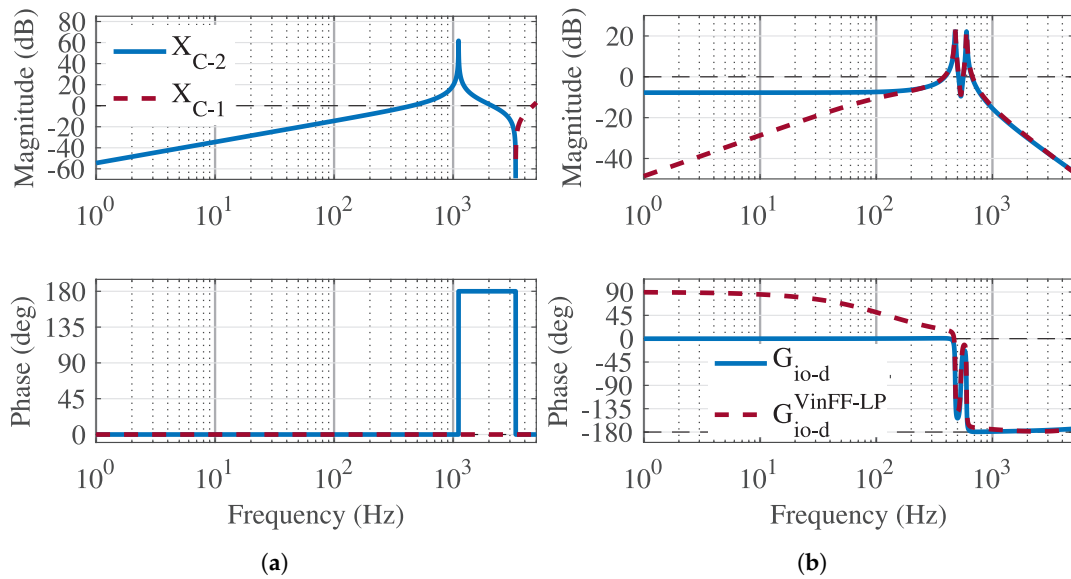


Figure 6. (a) Solutions X_{C-1} and X_{C-2} for the low-pass filter related to the input-to-output dynamics. (b) Input-voltage feedforward-affected input-to-output dynamics d component with and without the low-pass filter.

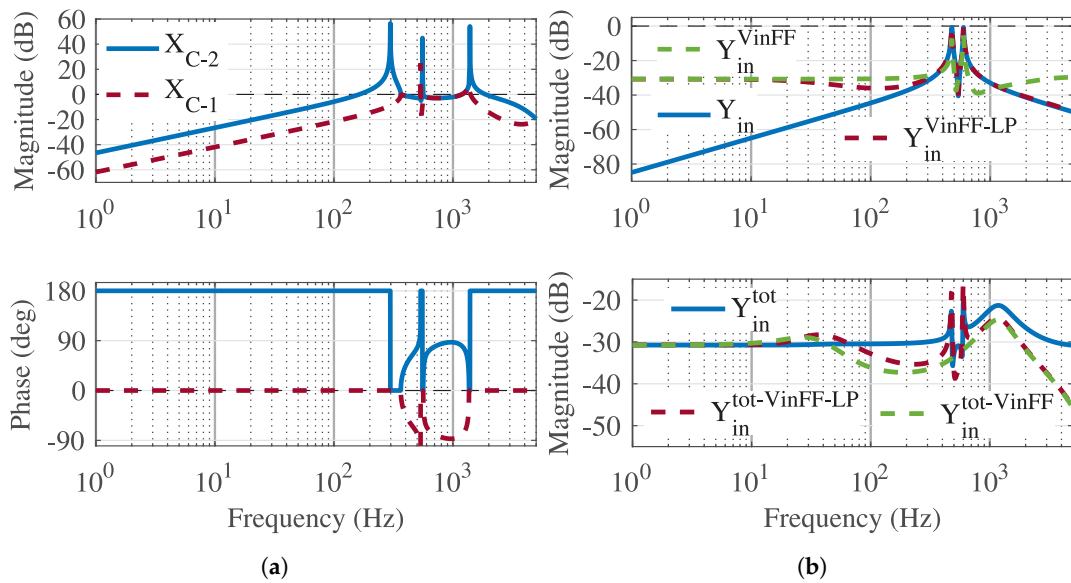


Figure 7. (a) Solutions X_{C-1} and X_{C-2} for the low-pass filter related to the input admittance. (b) Upper figure: comparison of the open-loop input admittance gain and lower figure: comparison of the closed-loop input admittance gain.

6. Experimental Verification

Figure 8 shows the setup of the system under study. The grid-forming inverter whose input-related dynamics are inspected is loaded by an active rectifier. The current i_{2-AFE} is controlled to make the load converter behave as a current sink. On the DC side, the voltage over a resistive load, v_{DC-AFE} , is controlled. However, during the frequency-response measurements at low frequencies, the DC-voltage controller was not used. The switching frequency used in the load converter is 20 kHz. The control system of the load converter was implemented by dSpace and the grid-forming inverter was controlled by a Imperix Boombbox. The parameters of the grid-forming inverter are given in Table 2. The voltage controller has the same PI-controller as in the analysis given in Sections 2–5. However, an additional low-pass filter is implemented at 500 Hz; therefore, the voltage controller is given by

$$G_{vc} = \frac{0.0398 + \frac{10}{s}}{\frac{s}{2\pi 500} + 1} \quad (40)$$

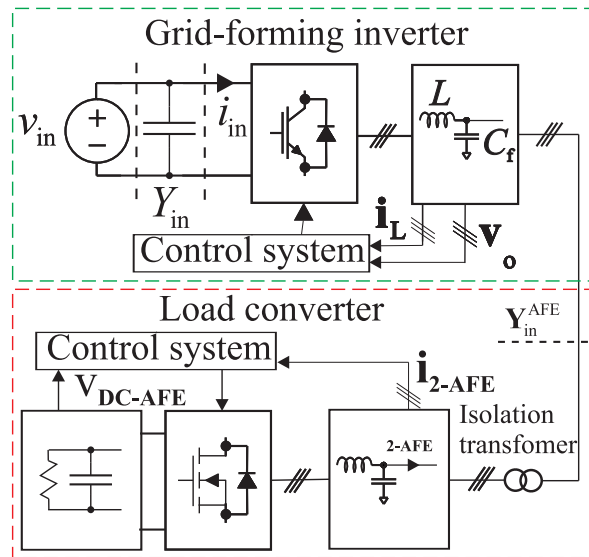


Figure 8. Block diagram of the laboratory setup.

Table 2. Experimental grid-forming inverter parameters and operating point values.

Parameter	Symbol	Value	Parameter	Symbol	Value
Input voltage	V_{in}	413 V	Input current	I_{in}	10.4 A
Output voltage d component	V_{od}	170 V	Output voltage q component	V_{oq}	0 V
Output current d component	I_{od}	16.5 A	Output current q component	I_{oq}	0 A
Switching frequency	f_s	8 kHz	Synchronous frequency	ω_s	$2\pi 60$ rad/s
Filter capacitor capacitance	C_f	30 μ F	Filter inductance	L	2.5 mH
C_f ESR and damping resistor	r_{Cf}	1.81 Ω	L ESR	r_L	0.065 Ω
Current controller P gain	K_{p-c}	0.028 Ω	Current controller I gain	K_{i-c}	17.8 VA ⁻¹ s ⁻¹
Voltage controller	G_{vc}	Equation (40)	DC capacitor capacitance	C_{DC}	750 μ F

In the experiments, the load converter is not an ideal current sink. Hence, there is an impedance-based interaction, and the load effect from the active rectifier must be considered [10,24]:

$$G_{io}^L = \left(\mathbf{I} + \mathbf{Z}_o \mathbf{Y}_{in}^{AFE} \right)^{-1} G_{io} \quad (41)$$

$$Y_{in}^L = Y_{in} + \mathbf{T}_{oi} \mathbf{Y}_{in}^{AFE} \left(\mathbf{I} + \mathbf{Z}_o \mathbf{Y}_{in}^{AFE} \right)^{-1} G_{io} \quad (42)$$

where Y_{in}^{AFE} is the AC input-admittance of the active rectifier, and the active rectifier is modeled by similar principles that have been used to model grid-connected PV inverters [4]. The superscript “L” is used to denote load-affected dynamics (the superscript is omitted in Figure 9 for simplicity).

Figure 9a,b show the measured frequency responses related to the closed-loop input-to-output dynamics and input admittance, respectively. The load-affected model clearly models well the input-to-output dynamics and the input admittance. The effect of the input-voltage feedforward is clearly visible in the closed-loop input-to-output dynamics d component, G_{io-d}^{tot} . The low-pass filter has only a minor effect on the high-frequency magnitude in G_{io-d}^{tot} . Therefore, the low-pass filter is not a good solution to reduce the detrimental effect in high frequencies. If the DC-capacitance, that is commonly used in the DC link, is included with the input admittance, the gain increases significantly

at low frequencies so that the input-voltage feedforward makes no significant difference with the used DC capacitor size.

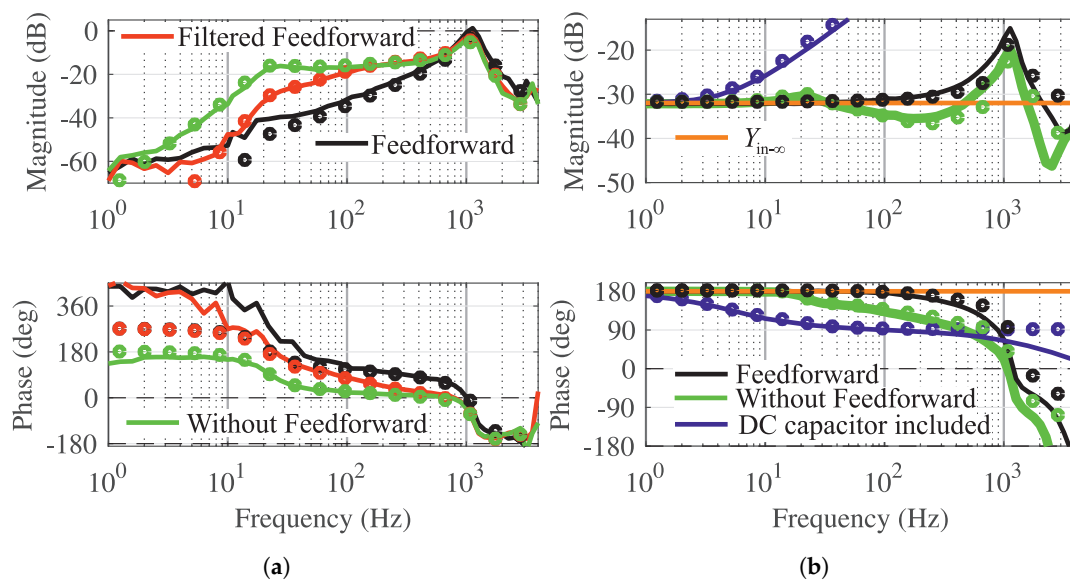


Figure 9. (a) Modeled (dots) and experimental (line) closed-loop input-to-output dynamics d component. (b) Modeled (dots) and experimental (line) closed-loop input admittance.

7. Analysis of the Proposed Model

This section compares the proposed ideal input admittance to existing ideal input admittance elements. It is shown that the existing model can be extracted from the proposed model.

Recently, a transfer-matrix representation for an ideal input admittance has been given [24] as:

$$\mathbf{Y}_{in-\infty} = \begin{bmatrix} Y_{in-\infty-d} & Y_{in-\infty-qd} \\ Y_{in-\infty-dq} & Y_{in-\infty-q} \end{bmatrix} = \begin{bmatrix} Y_{in} - \frac{G_{io-d}G_{ci-d}}{G_{co-d}} & Y_{in} - \frac{G_{io-d}G_{ci-q}}{G_{co-qd}} \\ Y_{in} - \frac{G_{io-q}G_{ci-d}}{G_{co-dq}} & Y_{in} - \frac{G_{io-q}G_{ci-q}}{G_{co-q}} \end{bmatrix} \quad (43)$$

The model in [24] is used as a tool to analyze the source-affected control-to-output dynamics of a three-phase grid-forming inverter in the DQ domain. In the present paper, the proposed ideal input admittance (19) is a scalar function that can be measured from a real system when the input-voltage feedforward is used. The presentation in (19) can be used to form the elements in $\mathbf{Y}_{in-\infty}$ in [24]. The key to solving the elements is to choose corresponding elements from the transfer matrices in (19) before any mathematical operations including the inverse of \mathbf{G}_{co} :

$$Y_{in-\infty-(m,n)} = Y_{in} + \mathbf{G}_{ci}(m) [\mathbf{G}_{co}(m,n)]^{-1} \mathbf{G}_{Vin}^{FF}(n) \quad (44)$$

where m and n are the elements of the matrices and vectors.

The expression in (44) links the proposed model to the existing application [24] of the extra element theorem in the dynamic analysis of three-phase converters. The findings of this study indicate that for a three-phase inverter $Y_{in-\infty}$ can be defined in addition to (43) [24].

8. Conclusions

The input-voltage feedforward control is widely used in power-electronic converters to prevent deviations in the DC input voltage appearing in the converter output. However, the feedforward implementation in three-phase converters has not been modeled in detail. This paper has proposed a dynamic of a three-phase grid-forming inverter utilizing the input-voltage feedforward.

The model accurately represents the feedforward-affected input admittance and the input-voltage-to-output-voltage dynamics. The gain in the input-voltage-to-output-voltage dynamics is significantly reduced by the feedforward. However, our study shows in detail that the feedforward does not provide an ideal decoupling from the input-voltage deviations due to the delay. The delay causes a detrimental effect at high frequencies, and the study shows that a minor improvement can be achieved by low-pass filtering the feedforward control signal.

The input admittance is affected detrimentally by the feedforward. This paper has demonstrated that the unterminated input admittance can be approximated well by the ideal input admittance which corresponds to an inverter with an infinite fast output-voltage controller. However, if the DC capacitor is considered as a part of the admittance, the input admittance shape could be dictated by the capacitor admittance.

The proposed model can be applied to the impedance-based stability analysis at the DC interface of three-phase inverters and to analyze the effect of the deviations in the DC voltage to the AC voltage.

Author Contributions: Conceptualization, M.B.; Formal analysis, M.B.; Investigation, M.B.; Supervision, T.R.; Validation, M.B.; Writing—original draft, M.B.; Writing—review & editing, T.R. All authors have read and agreed to the published version of the manuscript.

Funding: This research received external funding from Business Finland project SolarX.

Conflicts of Interest: The authors declare no conflicts of interest

References

1. Yang, D.; Wang, X. Unified modular state-space modeling of grid-connected voltage-source converters. *IEEE Trans. Power Electron.* **2020**, *35*, 9702–9717. [[CrossRef](#)]
2. Wen, B.; Boroyevich, D.; Burgos, R.; Mattavelli, P.; Shen, Z. Small-signal stability analysis of three-phase AC systems in the presence of constant power loads based on measured d-q frame impedances. *IEEE Trans. Power Electron.* **2015**, *30*, 5952–5963. [[CrossRef](#)]
3. Lu, D.; Wang, X.; Blaabjerg, F. Impedance-based analysis of DC-link voltage dynamics in voltage-source converters. *IEEE Trans. Power Electron.* **2019**, *34*, 3973–3985. [[CrossRef](#)]
4. Aapro, A.; Messo, T.; Roinila, T.; Suntio, T. Effect of active damping on output impedance of three-phase grid-connected converter. *IEEE Trans. Ind. Electron.* **2017**, *64*, 7532–7541. [[CrossRef](#)]
5. Unamuno, E.; Rygg, A.; Amin, M.; Molinas, M.; Barrena, J.A. Impedance-based stability evaluation of virtual synchronous machine implementations in converter controllers. In Proceedings of the 2018 International Power Electronics Conference (IPEC-Niigata 2018 -ECCE Asia), Niigata, Japan, 20–24 May 2018; IEEE: Piscataway, NJ, USA, 2018; pp. 759–766.
6. Xue, D.; Liu, J.; Liu, Z.; Tu, Y.; Liu, T. Modeling and analysis of DC terminal impedance of voltage-source converters with different control modes. *IEEE Trans. Power Electron.* **2020**, *35*, 5883–5896. [[CrossRef](#)]
7. Moradi-Shahrbabak, Z.; Tabesh, A. Effects of front-end converter and DC-link of a utility-scale PV energy system on dynamic stability of a power system. *IEEE Trans. Ind. Electron.* **2018**, *65*, 403–411. [[CrossRef](#)]
8. Wang, R.; Wu, Y.; He, G.; Lv, Y.; Du, J.; Li, Y. Impedance modeling and stability analysis for cascade system of three-phase PWM rectifier and LLC resonant converter. *Energies* **2018**, *11*, 3050. [[CrossRef](#)]
9. Radwan, A.A.A.; Mohamed, Y.A.R.I.; El-Saadany, E.F. Assessment and performance evaluation of DC-side interactions of voltage-source inverters interfacing renewable energy systems. *Sustain. Energy Grids Netw.* **2015**, *1*, 28–44. [[CrossRef](#)]
10. Berg, M.; Messo, T.; Suntio, T. Frequency response analysis of load effect on dynamics of grid-forming inverter. In Proceedings of the 2018 International Power Electronics Conference (IPEC-Niigata 2018 -ECCE Asia), Niigata, Japan, 20–24 May 2018; pp. 963–970.
11. Bogdanov, D.; Ralchev, M.; Mateev, V.; Marinova, I. Harmonic spectrum filtration for current sensor measurements. In Proceedings of the 2019 16th Conference on Electrical Machines, Drives and Power Systems (ELMA), Varna, Bulgaria, 6–8 June 2019.
12. Karppanen, M.; Sippola, M.; Suntio, T. Dynamics of input-voltage-feedforward-controlled buck converter. In Proceedings of the INTELEC 06-Twenty-Eighth International Telecommunications Energy Conference, Providence, RI, USA, 10–14 September 2006; IEEE: Piscataway, NJ, USA, 2006; pp. 1005–1013.

13. Karppanen, M.; Suntio, T.; Sippola, M. Dynamical characterization of input-voltage-feedforward-controlled buck converter. *IEEE Trans. Ind. Electron.* **2007**, *54*, 1005–1013. [[CrossRef](#)]
14. Jia, P.; Zheng, T.Q.; Li, Y. Research on input-voltage feedforward control for high-order converter topologies. *IET Power Electron.* **2014**, *7*, 2778–2790.
15. Ramezani, M.; Li, S.; Golestan, S. Analysis and controller design for stand-alone VSIs in synchronous reference frame. *IET Power Electron.* **2017**, *10*, 1003–1012. [[CrossRef](#)]
16. Han, Y.; Shen, P.; Zhao, X.; Guerrero, J.M. Control strategies for islanded microgrid using enhanced hierarchical control structure with multiple current-loop damping schemes. *IEEE Trans. Smart Grid* **2017**, *8*, 1139–1153. [[CrossRef](#)]
17. Suul, J.A.; D’Arco, S.; Rodríguez, P.; Molinas, M. Impedance-compensated grid synchronisation for extending the stability range of weak grids with voltage source converters. *IET Gener. Transm. Distrib.* **2016**, *10*, 1315–1326. [[CrossRef](#)]
18. D’Arco, S.; Suul, J.A.; Fosso, O.B. A virtual synchronous machine implementation for distributed control of power converters in smartgrids. *Electr. Power Syst. Res.* **2015**, *122*, 180–197. [[CrossRef](#)]
19. Mo, O.; Darco, S.; Suul, J.A. Evaluation of virtual synchronous machines with dynamic or quasi-stationary machine models. *IEEE Trans. Ind. Electron.* **2017**, *64*, 5952–5962. [[CrossRef](#)]
20. Kroutikova, N.; Hernandez-Aramburo, C.; Green, T. State-space model of grid-connected inverters under current control mode. *IET Electr. Power Appl.* **2007**, *1*, 329. [[CrossRef](#)]
21. Vesti, S.; Suntio, T.; Oliver, J.A.; Prieto, R.; Cobos, J.A. Effect of control method on impedance-based interactions in a buck converter. *IEEE Trans. Power Electron.* **2013**, *28*, 5311–5322. [[CrossRef](#)]
22. Suntio, T. *Dynamic Profile of Switched-Mode Converter: Modeling, Analysis and Control*; Wiley-VCH: Weinheim, Germany, 2009.
23. Suntio, T.; Messo, T.; Puukko, J. *Power Electronic Converters: Dynamics and Control in Conventional and Renewable Energy Applications*; Wiley-VCH: Weinheim, Germany, 2017.
24. Suntio, T.; Messo, T.; Berg, M.; Alenius, H.; Reinikka, T.; Luhtala, R.; Zenger, K. Impedance-based interactions in grid-tied three-phase inverters in renewable energy applications. *Energies* **2019**, *12*, 464. [[CrossRef](#)]
25. Middlebrook, R. Null double injection and the extra element theorem. *IEEE Trans. Educ.* **1989**, *32*, 167–180. [[CrossRef](#)]
26. Zou, C.; Rao, H.; Xu, S.; Li, Y.; Li, W.; Chen, J.; Zhao, X.; Yang, Y.; Lei, B. Analysis of resonance between a VSC-HVDC converter and the AC grid. *IEEE Trans. Power Electron.* **2018**, *33*, 10157–10168. [[CrossRef](#)]
27. Middlebrook, R.D. The N Extra Element Theorem. *IEEE Trans. Circuits Syst. I Fundam. Theory Appl.* **1998**, *45*, 919–935. [[CrossRef](#)]
28. Guest, E.; Jensen, K.H.; Rasmussen, T.W. Mitigation of harmonic voltage amplification in offshore wind power plants by wind turbines with embedded active filters. *IEEE Trans. Sustain. Energy* **2020**, *11*, 785–794. [[CrossRef](#)]

